

**STUDY OF THE EFFECT OF SINTERING PARAMETERS ON  
CHARACTERISTICS OF W-BRONZE COMPOSITES PREPARED VIA  
DIFFERENT DENSIFICATION TECHNIQUES**

by

**KAHTAN S. MOHAMMED**

**Thesis submitted in fulfilment of the  
requirements for the degree  
of Doctor of Philosophy**

**Universiti Sains Malaysia**

**2010**

## AKNOWLEDGEMENTS

Great thanks to Almighty Allah who granted me health, patience, capability and knowledge to execute this study.

I would like to express my sincere gratitude profoundly from my heart for the fruitful assistance, guidance and encouragement of my supervisor Associate Professor Dr. Azmi Bin Rahmat. Many thank and gratitude to my co-supervisor Dr. Ahmad Badri Ismail, for his constant support. The deepest gratitude to my late mentor Associate Professor Dr. Luay Bakir Hussain (Allah rest his soul) for his trusted and valuable advice. I would like to extend my gratefulness to Associate Professor Dr. Azizan Aziz and Professor Radzali Othman for their assistance and valuable discussions. I am also grateful to Professor Ahmad Fauzi Mohd Noor and the administrative staff of the School of Materials and Mineral Resources Engineering for their support.

I gratefully acknowledge the support provided by the Tin Technology UK (ITR), Malaysian Smelting Corporation (MSC) and the Universiti Sains Malaysia for the financial support, which made the presentation of this work possible. I highly appreciate the outstanding efforts of Mrs. Fong, Mr. Sharhrul and Mr. Rashid. I wish to acknowledge the assistance of the laboratory technical staffs: Mr. Helmi, Mr. Azam, Kemuridan, Mokhtar, Haleem, Mr. Shahid, Mr. Zaini, Mr. Razak, Mr. Farid and Mr. Khairi.

Finally, I dedicate this work to my beloved wife, Haiba, who had been extremely supportive of me and shouldered the burdens of the family during my absence.

Kahtan S. Mohammed

## CONTENTS

	<b>PAGE</b>
ACKNOWLEDGMENT	ii
TABLE OF CONTENTS	iii
LIST OF TABLES	vii
LIST OF FIGURES	viii
LIST OF PLATES	xxiii
LIST OF ABBREVIATION	xxiv
LIST OF APPENDICES	xxvi
LIST OF PUBLICATIONS & SEMINARS	xxvii
ABSTRAK	xxviii
ABSTRACT	xxvi
<b>CHAPTER 1: INTRODUCTION</b>	<b>1</b>
1.1 Tungsten-Bronze Composite	3
1.2 Importance of Study	4
1.3 Problem Statement	5
1.4 Objective of Study	6
1.5 Scope of study	7
1.5 Structure of the Thesis	8
<b>CHAPTER 2 : LITERATURE REVIEW</b>	<b>9</b>
2.1 Powder Metallurgy	9
2.2 Liquid Phase Sintering (LPS)	9
2.2.1 Initial Stage	11

2.2.2	Intermediate Stage	12
2.2.3	Final Stage	14
2.2.4	Grain Growth	14
2.3	Supersolidus Liquid Phase Sintering (SLPS)	15
2.4	Activated Sintering	19
2.4.1	Activated Sintering by Transition Metal Addition	20
2.4.2	Mechanically Activated Sintering	28
2.4.2.1	Mechanism of Mechanical Alloying	30
2.5	Infiltration Techniques	34
2.5.1	Forced Infiltration	35
2.6	Wetting Angle and Capillary Force	39
2.7	Contiguity	42
2.8	Connectivity and Dihedral Angle	42
2.9	Mechanical Properties	44
2.9.1	Wear	45
2.9.2	Transverse rupture and compression strength	46
2.10	Physical properties	47
2.10.1	Electrical conductivity	47
2.10.2	Thermal expansion	48
2.11	Material and Their Properties	46
2.11.1	Tungsten (W)	49
2.11.2	Copper (Cu)	50
2.11.3	Tin (Sn)	50
2.11.4	Bronze	51
2.12	Swelling	50

2.13 Phase Diagrams	52
2.13.1 Cu-Sn Phase Diagram	52
2.13.2 Cu-W Phase Diagram	53
2.13.3 Cu-Fe Phase Diagram	54
2.13.4 Fe-W Phase Diagram	54
2.13.5 Fe-Sn Phase Diagram	55
2.13.6 Co-Cu Phase Diagram	56
2.13.7 Co-W Phase Diagram	57
2.13.8 Co-Sn Phase Diagram	58
2.14 Corrosion of W-Bronze and Its Environmental Effects	59
2.15 Sintering atmosphere	61
<b>CHAPTER 3: MATERIALS, EQUIPMENT AND EXPERIMENTAL PROCEDURES</b>	<b>63</b>
3.1 Characterization of the Raw Materials	63
3.1.1 As Received Powders Used in the Study	64
3.2 Green Compaction	66
3.3 Sintering process	67
3.4 Density, Shrinkage and Densification Measurements	69
3.5 Microstructure Analysis of the Sintered Compacts	70
3.6 Activated Sintering by Transition Metals Addition	71
3.7 Mechanical Alloying by Ball Milling	72
3.8 Infiltration by Shell-On-Core Approach	75
3.9 Mechanical Properties	77
3.9.1 Wear Resistance	77

3.9.2	Microhardness Testing	79
3.9.3	Strength Testing	79
3.10	Corrosion Test	81
<b>CHAPTER 4: RESULTS AND DISCUSSION</b>		<b>83</b>
4.1	Characterization of the As Received Powders	83
4.1.1	SEM and EDX of the Raw Materials	83
4.1.2	Particle Size Measurement	88
4.1.3	Thermal Analysis	90
4.2	Mechanically Activated Sintering	96
4.3	SLPS, LPS And Activated Sintering	116
4.4	Infiltration by Shell-On-Core Approach	140
4.5	Mechanical properties	156
4.5.1	Wear Resistance	156
4.5.2	Transverse Rupture Strength	165
4.6	Physical Properties	173
4.6.1	Thermal Expansion	173
4.6.2	Electrical Conductivity	177
4.7	Corrosion Resistance	181
4.8	Sintering Atmosphere	195
<b>CHAPTER 5: CONCLUSIONS AND FUTURE WORKS</b>		<b>196</b>
5.1	Conclusions	200
5.2	Future Works	201
<b>REFERENCES</b>		
<b>APPENDICES</b>		

## LIST OF TABLES

	<b>PAGE</b>
Table 2.1 The solid content and fractional coverage of grain boundary by the liquid	16
Table 2.2 The solubilities of the activators in Cu and W at different temperatures	25
Table 2.3 Material used constants and properties	49
Table 3.1 Characteristics of the as received powders used in the study	64
Table 4.1 DSC plots analysis of Cu-Sn green compact	94
Table 4.2 The specifications of the four sintered compact sets, fabricated in this study	99
Table.4.3 Composition and properties of W-bronze samples	119
Table. 4.4 Physical parameters pertaining to the shell-on-core materials	156
Table 4.5 Density, microhardness and roughness values of the worn specimens	165
Table 4.6 Transverse rupture strength of different W-bronze specimens with their sintered densities and microhardness values	166
Table 4.7 Diametral compression test results of different W-bronze specimens with their sintered density and microhardness values	169
Table 4.8 The CTE values for W-bronze specimens of different composition and sintering conditions	168
Table 4.9 Electrical resistivity, conductivity and porosity level values for different W-bronze sintered compacts	174
Table 4.10 The chemical compounds of the corroded surfaces detected by XRD analysis	194

**LIST OF FIGURES**

	<b>PAGE</b>
Fig.2.1 Two-particle geometry for predicting densification during the initial stage of liquid-phase sintering. The model considers mass transport through a liquid layer of thickness $\delta$ with a grain size of $G$ , a neck radius of $x$ , and a curvature gradient at the neck of $r$ .	12
Fig.2.2 A cross-sectional view of the model microstructure for the intermediate stage of liquid-phase sintering	13
Fig. 2.3 Schematic phase diagram showing the solidus and liquidus as straight lines, providing a simple means to estimate the effect of temperature on the liquid content and densification for an alloy of composition $X_A$ in SLPS process	16
Fig.2.4 Two models of tungsten particles which have been coated with metallic activator, show different representations of the sintering process (a) Brophy, Hayden and Wulff model (b) Toth and Lockington model (Corti, 1986).	22
Fig. 2.5 Phase diagram of an ideal system for liquid-phase sintering and metal activated sintering (German, 1992).	24
Fig. 2.6 Refinement of particle and grain sizes with milling time. Rate of refinement increases with higher ball-to powder weight ratios (Lee, 1998).	31
Fig. 2.7 Steps of gas pressure infiltration process (a) porous preform above matrix material during heating (b) immersion of porous	35



perform into the molten matrix material and inlet of pressurized gas (c) infiltrated sample in molten matrix and (d) withdrawal of infiltrated sample from the melt.

Fig. 2.8	A sessile drop to the left is an example of poor wetting ( $\theta > 90^\circ$ ) and the sessile drop to the right is an example of good wetting $\theta < 90^\circ$	40
Fig. 2.9	The capillary adhesion force sticks two plates wetted by water droplet mashed between them	41
Fig. 2.10	The dihedral angle and surface energy equilibrium between intersecting grains with a partially penetrating liquid phase	43
Fig. 2.11	Effect of the dihedral angle on the critical solid volume fraction for freestanding structural rigidity	44
Fig. 2.12	Copper-tin phase diagram	52
Fig. 2.13	Copper-Tungsten phase diagram	53
Fig. 2.14	Iron-Copper phase diagram	54
Fig. 2.15	Iron-Tungsten phase diagram	54
Fig. 2.16	Iron-Tin phase diagram	56
Fig. 2.17	Cobalt-copper phase diagram	57
Fig. 2.18	Cobalt-Tungsten phase diagram	58
Fig. 2.19	Cobalt-Tin phase diagram	59
Fig. 3.1	Flow chart indicating the research outline activities	65
Fig. 3.2	The temperature-time sintering program.	69
Fig. 3.3	Flow chart of the two-step ball milling procedure.	75
Fig. 4.1	SEM images with EDX analyses of (a) W powder (b) annealed bronze powder (c) Sn powder.	84

Fig. 4.2	SEM and EDX analysis of (a) Cu powder (b) Co powder (d) Fe powder, oxidation and carbon content in Co are attributed to storage environment and production conditions.	85
Fig. 4.3	SEM images of (a) the W50wt.%-Sn mixture after the first step of the “Two-step BM process” (b) the final product W50wt.%-pre-mix bronze mixture after the second step of the “Two-step BM process” of (c) the final product of W50wt.%-pre-alloy bronze of one-step BM powder mixture.	86
Fig. 4.4	SEM images of (a) W40wt.%-pre-alloy bronze (b) W40wt.%-pre-alloy bronze-Fe5wt.% (c) compact of two-step W50wt.%-pre-mix bronze BM powder (d) compact of one-step W50wt.%-pre-alloy bronze BM powder.	87
Fig. 4.5	Particle size distribution of (a) tungsten powder (b) tin powder (c) copper powder.	89
Fig. 4.6	Particle size distribution of (a) annealed bronze powder (b) W50wt.%-pre-mix bronze BM powder (c) W50wt.%-pre-alloy BM bronze powder.	90
Fig. 4.7	DSC and TG of (a) Cu-Sn green compact (b) W50wt.%-Cu-Sn10wt.% BM in WC jar for 25 h (c) W50wt.%-Cu-Sn10wt% BM steel jar for 25 h.	92
Fig. 4.8	XRD plots of two-step W50wt.%-pre-mix bronze powders BM in different jar types.	95
Fig. 4.9	XRD plots for two-step W50wt.% pre-mix bronze and one-step W50wt.%-pre-alloy bronze.	96
Fig. 4.10	The relative sintered density of the four sintered compact sets,	100

the two-step W50wt.%-pre-mix bronze showed the highest sintered density.

- Fig. 4.11 (a) Hardness profiles (b) densification of the four sintered compact sets. Specimens of the two-step BM process showed the highest densification. 100
- Fig.4.12 XRD analysis of different mixes of the two-step BM W50wt.%-pre-mix bronze powder at different BM stages, (a) as received W50wt.%-5wt.%Sn before BM (b) after BM for 8 hours (c) after BM for 15 hours (d) after the addition of Cu (e) after over all BM for 25 hours (f) the final sintered compact of W50wt.%-pre-mix bronze. 101
- Fig 4.13 The low magnification (X2) optical graphs of the four sintered compact sets, compacts of two-step BM powder. 102
- Fig. 4.14 Low magnification SEM micrographs of the four different W50wt.%-bronze compacts sintered at 1150°C under H<sub>2</sub>/N<sub>2</sub> as protective gas.. 103
- Fig. 4.15 (a) and (b) are of two-step conventionally sintered compact of W50wt.%-pre-mix bronze (c) and (d) of inserted W50wt.%-pre-mix sintered compact (e) W50wt.%-pre-alloy bronze compact of BM powder sintered conventionally (f) W50wt.%-pre-alloy bronze inserted sintered compact. 105
- Fig.4.16 SEM micrograph of two-step W80wt.%-pre-mix bronze sintered at 1150°C showing very dense and homogenous structure of evenly distributed W grains in bronze structure. 106
- Fig. 4.17 W50wt.%-pre-alloy bronze of BM powder with 3wt.%Co 107

addition.

- Fig. 4.18 The main features of (a) two-step sintered compact structure shows thin bronze outer layer, sub layer of large W grains and high dense W-rich core (b) shows the effect of bronze liquid volume fraction on the thickness of the exuded outer shell layer at different sintering temperatures (c) and (d) show typical microstructure features of the sintered compacts of the two-step BM powders. 108
- Fig. 4.19 Schematic diagram represents the main forces acting on “a” W particle and the interaction with other b, c and d adjacent W particles during LPS, presuming that no W-W bonds are available and the liquid volume fraction is above 35%. 111
- Fig. 4.20 Microstructures of W50wt.%-pre-mix bronze sintered compacts with (a) Co3wt.% addition (b) Fe3wt.% addition sintered at 1000°C under vacuum. No signs of swelling are observed and promotion of grain growth and grain coalescence by activator addition is evident. 114
- Fig. 4.21 (a) SEM image of W50wt.%-pre-mix compact of BM powder, contamination of the BM powder by the steel milling media is prominent (b) and (c) show EDX spot scan indicate the existence of Fe element in the compact. Local big pores in the contaminated area are evident. 115
- Fig. 4.22 : SEM micrograph of (a) W40wt.% bronze-Fe2wt.%, (b) W40 wt.%-bronze-Fe 5wt.% and (c) Fe freeW40 wt.%-bronze, all 117

samples sintered at 965° C. the formation of Fe-W interdiffusion layer is evident in (a) and (b).

- Fig. 4.23 (a) SEM image coupled with EDX scan of W40wt.%-bronze-Fe3wt.% sintered compact shows the interdiffusion layer of  $Fe_7W_6$ , complete wetting is evident (b) Line EDX scan exhibits the richness of the interboundary layer in Fe element. 118
- Fig. 4.24 Superimposed XRD plots of W40wt.%-bronze of different Fe additions 120
- Fig. 4.25 The effect of (a) Fe additions on the green density of W10-40wt.%-bronze specimens (b) W and Fe contents on sintered density at sintering temperature of 900°C and under vacuum atmosphere (c) sintering temperature on density at different Fe additions. 122
- Fig. 4.26 (a) Effect of sintering temperature and sintering additives on densification (b) microhardness profile of W30wt.%-bronze with different Fe additions (c) effect of Fe addition on hardness of sintered compacts of different W contents. 123
- Fig. 4.27 Sintered compacts of W10-40wt%- bronze with Fe additions sintered at 980°C under  $H_2/N_2$  of 20/80 wt. ratio as protective gas. 125
- Fig. 4.28 (a) Effects of Fe and Co addition on W50wt.%-pre-alloy bronze sintered at 1100 and 920°C under vacuum (b) W65wt.%-pre-alloy bronze with Fe addition sintered at 1100, 127

1200 and 1300°C under H<sub>2</sub>/N<sub>2</sub> environment.

- Fig. 4.29 W50wt.%-pre-alloy bronze sintered at 920°C for 10 hours under H<sub>2</sub>/N<sub>2</sub> environment 128
- Fig. 4.30 SEM images (a) W40wt.%-bronze- Fe3wt% sintered at 900°C, vacuum (b) W40wt.%-bronze- Fe2wt.% sintered at 965°C H<sub>2</sub>/N<sub>2</sub> (c) W40wt.%-bronze-Fe5wt.% sintered at 965°C (d) W80wt.%-bronze-Fe2wt.% sintered at 1300 H<sub>2</sub>/N<sub>2</sub>. (a), (b), (c) and (d) represent the four stages involved in W dissolution and the final formation of Fe-rich-W phase equilibrium composition. 130
- Fig.4.31 SEM images of (a) W50-bronze-Co3wt.% sintered at 920°C, vacuum(b) W50-bronze-Co3wt.% sintered at 1150°C under H<sub>2</sub>/N<sub>2</sub> gas (c) W40-bronze-Co3wt.% sintered at1150 °C H<sub>2</sub>/Ar gas of 5/95 wt. ratio(d) W65-bronze-Co3wt% sintered at1300 °C under H<sub>2</sub>/N<sub>2</sub> gas. Grains of grey contrast in (d) are of Co-rich-W phase of equilibrium composition. 132
- Fig. 4.32 (a) The effects of Fe activator and sintering temperature on grain growth of W40wt.%-pre-alloy bronze (b) The effect of Co activator on W grain growth of W50wt.%-pre-alloy bronze. 133
- Fig. 4.33 (a) Pure W+20 at. % Ni, Gupta *et al.*, 2007(b) W50wt.%-bronze-Co<sub>3</sub> of this study(c) computed lines of IGFs 138
- Fig. 4.34 Schematic representation of the present invention on its ongoing action. As the skin of the outer shell solidifies, it shrinks, displaces and compresses gradually towards the center, the builds up stress is driven by the differential coefficients of 142

thermal expansion ( $\Delta\text{CTE}$ ) of the shell and the core.

- Fig. 4.35 Simplified 3D schematic representation of the shell-on-core sintering concept. 143
- Fig. 4.36 Cross sections of core-on-shell infiltrated sintered compacts (a) of as received W80wt%-pre-mix bronze powder (b) of as received W40wt%-pre-mix bronze powder. The two compacts were sintered at 1150°C. 144
- Fig. 4.37 Different SEM micrographs of W80wt%-pre-mix bronze samples of as r. powders (a), (b) and (c) are of compacts sintered by the shell-on-core technique, (d), (e) and (f) are of compacts of similar composition but conventionally sintered. All compacts were die pressed under 350 MPa and sintered at 1150°C. 147
- Fig. 4.38 Shows the optical micrographs of (a) W80wt%-pre alloy bronze of as received powders sintered by conventional method (b) similar composition sintered by shell-on-core technique (c) and (d) W90wt%-pre-mix bronze samples sintered conventionally and by shell-on-core technique respectively. 148
- Fig. 4.39 (a) W50wt%-pre-alloy bronze compact of MA powder sintered by conventional method (b) similar compact densified by the shell/core technique (c) and (d) are two-step MA W50wt%-pre-mix bronze compacts, the former is sintered conventionally, the latter is by shell-on-core method, (e) and (f) show Line EDX at shell/core interface of both compact types. 149
- Fig. 4.40 Swelled sintered compact of W50wt%-pre-mix bronze of MA 150

powder. The compact is set as a core in pre-mix bronze shell and the swelling is due to Kirkendall effect.

- Fig. 4.41 W80wt%-pre-mix bronze compacts, (a) and (b) of 30°C/min. cooling rate (c) and (d) of 4°C/min. cooling rate. 151
- Fig. 4.42 (a) W80wt.%-pre-alloy bronze compact sintered by shell-on-core technique (author) (b) W preform infiltrated by melted Cu, utilizing the latest technology (Das, J. *et al.*, 2008). 152
- Fig. 4.43 Microhardness profile across W80wt.%-pre-mix bronze core encircled by pre-mix bronze shell. 153
- Fig. 4.44 Typical sintering program suitable for densification of W-bronze compacts by shell-on-core technique. 153
- Fig. 4.45 The radial displacement  $u(r)$  in the shell-on-core sphere of radius  $r = b$  for  $T = 770^\circ\text{C}$  and the core to shell concentration of  $c = (a^3/b^3) = 0.0156$  ( $a/b = 0.25$ ). The displacement is given by equations (4.4), (4.6) and (4.8) and the illustrated location of the elastic zone interface at  $r = R$ . 156
- Fig. 4.46 Plots of (a) different w content specimens, higher W content specimens show higher hardness and consequently lower wear rates (b) W40-bronze specimens of different Fe additions(c) roughness measurements of different W content worn specimens (d) typical temperature evolution during wear test of W-bronze specimens. 159
- Fig. 4.47 SEM images of (a) the worn surface of W10wt%-pre-alloy bronze compact (b) worn surface of W40wt%-pre-alloy bronze. (c) The line EDX reveals elemental analysis of the worn surface 160



(d) the area EDX analysis of the worn fractured delaminated patch of the sintered compact in (b).

- Fig. 4.48 (a) The wear of W-bronze specimens of different W contents 160  
(b) the effect of sliding speed on wear of W90-pre-mix bronze specimens fabricated by shell-on-core technique.
- Fig.4.49 Worn surfaces of W80wt%-pre-mix bronze samples(a) of as 161  
received powder (b) of MA powder.
- Fig. 4.50 W90wt%-pre-mix-bronze of as r powder (a) the surface of 163  
specimen worn at  $1.7 \text{ m s}^{-1}$  sliding speed (b) specimen worn at  $2.8 \text{ m s}^{-1}$  sliding speed.
- Fig. 4.51 (a) Shows wear debris of different particle shapes, bright 164  
appearance of some particles reveals poor conductivity of the debris heaps (b) the debris spot EDX analysis, high O and Fe elements reveal the dominance of oxidation wear mechanism. The debris was collected from different worn specimens of W content with 2wt.% Fe addition after  $50 \times 10^3 \text{ m}$  sliding distance.
- Fig. 4.52 (a) SEM image of the worn surface of the steel counter body, 164  
rubbing of the counter body surface by the edges of some protruded W particles on the specimen surface yields trapped and detached patches (b) the spot EDX analysis of adhered patch taken after 200 km of sliding distance.
- Fig. 4.53 The TRS test (stress versus strain) of W50wt%-pre-alloy 167  
bronze specimen sintered at  $1050^\circ\text{C}$  under argon.
- Fig. 4.54 The TRS of W50wt%-pre-mix bronze specimens sintered at 168

different environments and conditions. The specimen of two-step BM powder showed the highest rupture strength, density and hardness.

- Fig.4.55 The fractured surface of W50wt%-pre-mix specimen of two-step BM powder, W-W intergranular and W-matrix interface rupture fracture mechanisms are very evident 168
- Fig. 4.56 The SEM image of (a) fracture surface of W60wt.%-pre-mix bronze shows porous structure of weak cracked W-W and W-M bonds (b) fractured surface of W50wt.%-pre-mix bronze specimen exhibits fracturing mechanisms. 171
- Fig. 4.57 Fig. 4.56 The SEM fractographs of (a) W50-pre-mix bronze specimen (b) W50-pre-mix bronze specimen of 3wt%Fe additions. Fe addition improves TRS value. 172
- Fig. 4.58 Measured and calculated CTE values of different W content bronze specimens. Only specimen of W50wt.% was sintered under different temperature and furnace environment. 175
- Fig. 4.59 The thermal linear expansion of different W50wt.%-bronze specimens, specimens of BM powder showed lower CTE values. Above 400°C, the plots start losing their linearity. 175
- Fig. 4.60 The thermal expansion plots of the three W50wt.%-bronze specimens, show plot portions at elevated temperature, > 475°C, the plots lose their linearity and shoot up. 176
- Fig. 4.61 The SEM images of electrical conductivity test specimens (a) the W80wt.%-pre-mix bronze specimen, densified by the shell-on-core technique, showed the highest conductivity value (b) 179

W50wt.%-pre-mix bronze specimen of two-step BM powder showed better conductivity as opposed to W50wt.%-pre-alloy bronze specimen of one-step BM powder of (c).

- Fig.4.62 The electrical resistivity of different W-bronze specimens sintered under similar sintering conditions but by different techniques. Specimens sintered by shell-on-core technique (infiltrated), showed relatively low resistivity. 180
- Fig. 4.63 W50wt.%-bronze specimens of different starting material sintered at 1150°C for 3 hours under H<sub>2</sub>/N<sub>2</sub> gas. The specimen of two-step BM powder showed better resistivity as opposed to other, similar composition specimens. 181
- Fig. 4.64 Shows the effect of Fe addition on the corrosion rate of W20wt.%-bronze specimens at different exposure periods. 182
- Fig. 4.65 Different W20wt.%-bronze-Fe corroded specimens (a) Fe free specimen covered with bronze patina (b) EDX scan shows patina chemical analysis(c) and (d) specimen of Fe3wt.% additon, less chloride element is evident (e) and (f) specimen with 5wt.%Fe addition, different shapes of released particles are evident. Additionally, the extent of solid-state diffusion of W-W component (contiguity) could has some effects as well. 184
- Fig.4.66 Optical graph of W10wt%-bronze specimen reveals the appearance of the green patina layer which usually covers corroded specimens of high bronze content. 185
- Fig. 4.67 The effect of sintering temperature on corrosion of W40wt.%-bronze specimens with Fe5wt.% addition. Formation of W-Fe 185

grain interboundary layer and the extent of W dissolution in this layer are temperature dependent. This influences W-bronze galvanic potential and accordingly the corrosion rates.

- Fig. 4.68 Different W content Fe free corroded specimens (a) the metal weight loss at different exposure periods of specimens sintered at different temperatures (b) Fe free corroded W20wt.-%-bronze specimen of 7 days exposure, leaching of W to the surroundings is at early stage (c) specimen of W30wt.-%-pre-alloy bronze, the corroded and leached W particles are eminent (d) high Ca and Na are always connected to W release 186
- Fig. 4.69 Corrosion of different W content specimens at different exposure periods. 187
- Fig. 4.70 Different images of the corroded surface of W-bronze-Fe specimens (a) optical graph reveals the appearance of the specimen with Fe additions, dark brown and red spots are evident (b), (c) and (d) reveal the attacked W-Fe interdiffusion layer (e) and (f) corroded W element with Fe manifesting bloom-like structure of high Na and Ca elements. 189
- Fig 4.71 (a) Pure bronze specimen, W particles, from corrosion media are attached to the surface (b) corroded surface of W50-pre-alloy bronze specimen of MA powder (c) corroded surface of plate-like structure of the same specimen(d) EDX scan reveals high Ca and Na content. 190
- Fig. 4.72 The corrosion debris of W20wt.-%-bronze compacts (a) debris of Fe free specimens, debris composition are mainly tungsten 191

oxides with high Sn bronze patina particles (b) The EDX scan analysis (c) debris of specimens have Fe addition, the white color indicates high W content (d) EDX scan reveals the existence of W, Fe, Na and Ca and their oxides in the debris particles.

- Fig. 4.73 XRD plots of three W40-pre-alloy bronze specimens of different corrosion exposure periods, CuCl compound disappeared at long corrosion exposure period. 193
- Fig. 4.74 The sintered densities of W50wt.%-pre-mix bronze and W50-pre-alloy bronze specimens under different furnace atmospheres Sintering under vacuum and under nitrogen base gas gave the best results. 196
- Fig. 4.75 (a) The W80-pre-mix bronze specimen sintered at temperature of 1150°C with H<sub>2</sub>/N<sub>2</sub> as protective gas, the cooling down rate was 30°Cmin.<sup>-1</sup>. The high cooling rate promotes cracking of the oxidized W particle surface layer (b) EDX spot scan of the cracked particle shows high O content. 197
- Fig.4.76 The EDX spot scans of C and O elements measured on the vicinity region of W grain of W80wt.%-pre-mix bronze specimens sintered at 1150°C for 3 hours under different sintering atmospheres. Specimen sintered under argon atmosphere showed the highest oxygen content and the lowest sintered density. 199

## LIST OF PLATES

	<b>PAGE</b>
Plate 3.1 The powder compaction steel mould	66
Plate 3.2 The hydraulic press, maximum load of 14 tones	67
Plate 3.3 Sintering tube furnace of programmable logic controller	68
Plate 3.4 SEM coupled with EDX equipment	72
Plate 3.5 Attritor ball milling machine	74
Plate 3.6 Ceramics moulds	76
Plate 3.7 Spherical shell-on-core clump	77
Plate 3.8 Wear test machine	78
Plate 3.9 The wear counterpart	79
Plate 3.10 Three point transverse rupture strength standard test specimen	80
Plate 3.11 Axial torsion testing machine	81
Plate 3.12 Typical mode of fracture in Brazilian test (Jonsen and Haggblad, 2007).	81
Plate 3.13 Corrosion test assembly	82

## LIST OF ABBREVIATIONS

AES	Auger Electron Spectroscopy
ASTM	American Standard of Testing Materials
BM	Ball Milling
BS	British Standard
CTE	Coefficient of Thermal Expansion
$\Delta$ CTE	Differential Coefficients of Thermal Expansion
DCT	Diametral Compression Test
DSC	differential scanning calorimeter
EDX	Energy Dispersive X ray Analysis
FEVPSEM	Field Emission Variable Pressure Scanning Electron Microscopy
GP	Grain Boundary
HIP	Hot Isostatic Pressing
HRTEM	High Resolution Transmission Electron Microscopy
IGF	Intergranular Film
L/D	Pore Length and Pore Diameter ratio
LPS	Liquid Phase Sintering
MA	Mechanical Alloying
MMC	Metal Matrix Composite
MP	Melting Point
PD	Phase Diagram
PIM	Powder Injection Molding
PM	Powder Metallurgy
SEM	Scanning Electron Microscopy

SLPS	Supersolidus Liquid Phase Sintering
TD	Theoretical Density
TGA	thermogravimetric analyses
TRS	Transverse Rupture Strength
UD	Depleted Uranium
XRD	X ray Diffraction Analyses



## **LIST OF APPENDICES**

Appendix A	Journal paper
Appendix B	Patent No. PI 20093421
Appendix C	Proceeding 1
Appendix D	Proceeding 2
Appendix E	Proceeding 3
Appendix F	Proceeding 4
Appendix	Journal (under procedure)

## LIST OF PUBLICATIONS & SEMINARS

- 1.1 Kahtan S. Mohammad, Azmi Rahmat, Ahmad Badri Ismail. (2009) The effects of Fe additions on the liquid phase sintering of W-bronze composites. *Journal of Alloys and Compounds*. 482: 447-454.
- 1.2 Kahtan S. Mohammed, Azmi Bin Rahmat, Azizan Bin Aziz, (2009) A process for producing a metal-matrix composite of significant  $\Delta$ CTE between the hard base-metal and the soft matrix. Malaysian patent application No: PI 20093421.
- 1.3 M. Kahtan, H. B. Luay, R. Azmi, Ahmad Badri. (2007) The effect of temperature on the activated solid-state sintering of W-bronze-Fe heavy alloy. *Proceeding of the 6<sup>th</sup> Electron Microscopy Society Malaysia (EMSM) Scientific Conference, 10-12<sup>th</sup> December 2007 Pahang, Malaysia p30*.
- 1.4 M. S Kahtan R. Azmi and I. Ahmad Badri (2008) The effect of powder mixing techniques on the densification of W/bronze systems. *Proceeding of the 2<sup>th</sup> International Conference on Science & Technology Application in Industry & education, 12<sup>th</sup>-13<sup>th</sup> December 2008 at Universiti Technology Mara, Pulau Penang, Malaysia P40-41*.
- 1.5 M. S Kahtan R. Azmi and I. Ahmad Badri (2009) The factors affecting the swelling of W-bronze composite system at different sintering temperatures. *Proceeding of the 1<sup>st</sup> Regional Conference on Materials (RCM2009) 16<sup>th</sup>-17<sup>th</sup> February 2009, Pulau Penang, Malaysia, P55*.
- 1.6 M. S. Kahtan, R. Azmi and I. Ahmad Badri (2009) Sliding wear behavior of tungsten-bronze composites under different compositions and Fe sintering Additives. *Proceeding of the 4<sup>TH</sup> International Conference on Recent Advances in Materials, Minerals & Environment and 2<sup>nd</sup> Asian Symposium on Materials & processing. 1<sup>st</sup> -3<sup>rd</sup> June 2009, Penang, Malaysia, P113*.
- 1.7 M. S. Kahtan, R. Azmi and I. Ahmad Badri (2009) The effects of two-steps ball milling process on the liquid phase sintering of W-bronze composites. Paper to be published in the *Journal of Composites A*, under procedure, sent recently for Referee

**KAJIAN KESAN PARAMETER SINTERAN TERHADAP CIRI-CIRI  
KOMPOSIT W-GANGSA DISEDIAKAN MELALUI PELBAGAI TEKNIK  
PENUMPATAN**

**ABSTRAK**

Komposit W-gangsa ialah bahan komposit matriks logam yang mempunyai potensi yang baik. Ia mempunyai pelbagai potensi di dalam aplikasi ketenteraan dan industri dan ia boleh menggantikan plumbum dalam pelbagai bidang yang melibatkan ketumpatan sebagai pertimbangan utama. Dalam kajian ini, oleh kerana logam tungsten dan aloi gangsa adalah imisibel sepenuhnya di dalam kedua-dua fasa pepejal dan cecair, pelbagai pendekatan dan teknik telah digunakan untuk mendapatkan komposit yang mempunyai struktur kepadatan tinggi dan homogen. Persinteran fasa cecair solidus-lampau dengan tambahan 2 ke 3 % berat Fe meningkatkan kekerasan sebanyak dua kali ganda dan ketumpatan tersinter sebanyak 5 % ke 10%. Pengalioian mekanikal serbuk bahan mula W,Cu dan Sn dengan proses dua-peringkat menghasilkan partikel komposit W tertusuk di dalam matriks Cu-Sn. Hasil selepas persinteran adalah komposit yang mempunyai ketumpatan teori 85-95% ketumpatan dengan sifat kerintangan kakisan dan haus yang amat baik. Dengan melaksanakan teknik penumpatan “rangka-keatas-teras” yang baru dicadangkan, komposit berkomposisi berlainan dengan ketumpatan teori 95-99% ketumpatan teori komposits W-gangsa dapat dihasilkan. Bahan komposit W-gangsa yang berlainan dihasilkan dan dikenakan pelbagai ujian dan pemeriksaan di makmal untuk menilai sifat-sifat mikrostruktur, kepatahan, mekanikal, kimia dan fizikal. Kompaks W50% berat-pracampur gangsa tersinter pada 1050°C di bawah argon ia itu tanpa agen penurunan oksida memberikan kekerasan Vickers 237 dan kekuatan patah pindah

433MPa. Kompaks W40% berat-pra aloi gangsa dengan tambahan 2% berat Fe tersinter pada 900°C di bawah vakum menunjukkan kadar haus ter rendah  $2 \cdot 10^{-7} \text{ g.m}^{-1}$ . Kompaks W80% berat-pra aloi gangsa tersinter dan tertumpat dengan kaedah “rankga-keatas-teras” pada 1150°C di bawah gas  $\text{H}_2/\text{N}_2$  menunjukkan kerintangan terendah  $5.9 \mu\Omega\text{cm}$ . Pekali pengembangan termal terendah secara relatif ditunjukkan oleh kompaks W50% berat-pra aloi gangsa serbuk teraloi secara satu-peringkat mekanikal tersinter pada 1000 °C di bawah vakum. Kadar kakisan terendah telah ditunjukkan oleh kompaks W50% berat- pra aloi gangsa serbuk teraloi secara dua-peringkat mekanikal tersinter pada 1150 °C dalam gas  $\text{H}_2/\text{N}_2$ . Kompaks mengandungi W terendah secara relatif menunjukkan ketumpatan tersinter lebih baik bila disinter di bawah persekitaran vakum manakala kompaks mengandungi W tinggi (>70% berat) memberikan ketumpatan tersinter lebih baik bila disinter dibawah gas  $\text{H}_2/\text{N}_2$ .

**STUDY OF THE EFFECT OF SINTERING PARAMETERS ON  
CHARACTERISTICS OF W-BRONZE COMPOSITES PREPARED VIA  
DIFFERENT DENSIFICATION TECHNIQUES**

**ABSTRACT**

W-bronze composites are very promising MMC material. It has high potential in military and industrial applications and it can replace lead in different fields where the density is of main consideration. In this study, since tungsten metal and bronze alloy are almost completely immiscible in both solid and liquid phases, different approaches and techniques were utilized to attain highly dense and homogeneously structured composites. Super-solidus liquid phase sintering with 2 to 3 wt.% Fe additions improved the hardness by two folds and the sintered density by 5 % to 10%. Mechanical alloying of the W, Cu and Sn powder precursors by two-step process yielded composite particles of W impregnated in Cu-Sn matrix. The outcome after sintering was a composite of 85 to 95% of their theoretical density with excellent corrosion and wear resistance properties. By the implementation of a proposed new shell-on-core densification technique, composites of different compositions with 95-99% of their theoretical density were attained. The different W-bronze composite materials produced, were subjected to different laboratory testing and examinations to assess their microstructural, fractural, mechanical, chemical and physical properties. Compacts of W50wt%-pre mix bronze sintered at 1050°C under argon i.e with out oxide reduction agent gave Vickers hardness of 237 and transfer rupture strength of 433MPa. Compacts of W40wt%-pre-alloy bronze of 2wt.% Fe addition sintered at 900°C under vacuum showed the lowest wear rate of

$2 \times 10^{-7} \text{ gm}^{-1}$ . Compacts of W80wt%-pre-alloy bronze sintered and densified by shell-on-core technique at 1150 °C under  $\text{H}_2/\text{N}_2$  gas showed the lowest resistivity of  $5.9 \mu\Omega\text{cm}$ . Relatively lowest thermal expansion coefficient of  $12.8 \times 10^{-6} \text{ C}^{-1}$  was shown by W50wt.% pre-alloy bronze compact of one-step mechanically alloyed powder sintered at 1000°C under vacuum. Lowest corrosion rate of  $0.12 \text{ mg/m}^2\text{h}$  was manifested by W50wt.%-pre-alloy bronze compact of two-step MA powder sintered at 1150°C at  $\text{H}_2/\text{N}_2$  gas. Compacts of relatively low W contents showed better sintered density when sintered under vacuum environment while compacts of high W content ( $> 70\text{wt.}\%$ ) gave better sintered density when sintered under  $\text{H}_2/\text{N}_2$  gas.

## CHAPTER 1

### INTRODUCTION

In the last few decades metal matrix composites (MMCs) have generated considerable interest within material community. The “composite” approach to metallurgical processing is the only pathway for the production of entire new classes of metallic material. Due to their immiscibility in each other, aluminum, copper, or magnesium, only in this way can be combined with significant volume fractions of carbide, oxide, or nitride phases. This approach facilitates significant alterations and improvements in the physical and mechanical properties of metallic materials.

Characterized by their unique physical and mechanical properties, tungsten-copper (W-Cu) MMC has recently attracted great attention. W-Cu composites are typical *pseudo*-alloys combining the intrinsic properties of W and Cu constituents, their high strength; adequate fracture toughness; high hardness and high density make them very useful in military and industrial applications. The density is among the key factors determining the physical and mechanical performance of W-Cu parts which are ordinarily manufactured through powder metallurgy technology. Porosity free composite structure is highly recommended feature in any conventional sintering process. Porosity is deleterious to flexural strength, electrical and thermal conductivity of the composite. The pores and voids act as points of stress concentrations and reduce the cross-sectional area across which a load is applied and lead to a tremendous fall of the flexural strength. Air that is present in the pores has poor thermal and electrical conductivity and thus deteriorates the overall thermal and electrical properties of the composite (German, 1992).

There are many publications and researches cover the densification of tungsten-copper system and on the contrary, very few is available for tungsten-bronze system. The outcomes of the majority of these researches are not disclosed due to their military applications, especially those related to kinetic energy projectiles, ammunition and armor penetrators.

Bronze is a metal alloy consisting primarily of copper, usually with tin as the main additive. Bronze is typically 88wt.% copper and 12wt.% tin. Alpha bronze consists of the alpha solid solution of tin in copper. Bronze has very attractive properties; it is hard with enough ductility, has good corrosion resistance and good wear resistance (Turhan, 2005).

Pre-alloyed bronze powder usually melts over a range of temperatures. This feature is very useful in performing supersolidus liquid-phase sintering (SLPS) condition in bronze matrix composites. In SLPS the sintering temperature is between the liquidus and solidus (German, 1997). Accordingly, bronze offers a range of liquid phase volume fractions during sintering process. For bronze of 10wt% Sn, liquid phase starts forming at as low as 798 °C and higher, while for W-Cu system, the liquid phase sintering process usually performs at temperature at least higher than the melting temperature of Cu ( $T_m=1085^\circ\text{C}$ ).

On the other hand tungsten is an incredible material. It is dense and hard, and has the lowest vapor pressure and the highest melting temperature of all metals. It also has reasonably good erosion resistance and retains reasonable strength and elastic modulus at elevated temperatures but the inherent drawbacks of tungsten are its brittleness, poor machinability and formability (Das *et al.*, 2008). It has been



observed in practice that excellent properties could be imparted to tungsten when coupled with relatively soft metal like copper or pre-alloy bronze.

## **1.1 Tungsten-bronze Composites**

Composite materials of tungsten-bronze (W-bronze) are useful in a variety of applications where thermal and mechanical properties of bronze and the very low expansion characteristics and the high melting temperature of W can be advantageously utilized. The combinations of these elements even lead to the optimization of other alloy properties such as ductility, mechanical strength, and corrosion and wear resistance at elevated temperature.

Primary applications of these composite materials are for lead (Pb) replacement, ammunitions, waterfowl shots, weight balance adjusters, high density gyroscopic rotors, radiation shields and kinetic energy penetrators. W-bronze composites are identified as a potentially suitable material for electrical and electronic applications like electrical contactors especially at high voltages, resistance welding electrodes, electro-discharge machining electrodes.

W-bronze components are immiscible in each other. Accordingly, during liquid-phase sintering (LPS), W-bronze shrinks mainly via W particles rearrangement and attaining fully dense structures of this system by LPS is not viable. To tackle the similar problems in W-Cu composites, the researchers tried different techniques. These techniques comprise sintering at higher temperatures, using finer elemental powders and incorporating sintering activators Fe, Co, Ni and Pd (Johnson and German, 1993).

Other more sophisticated technique is to alter the surface morphology and the wettability of the W-base metal by thin film Ni coatings of the W particles prior to sintering or to mechanically alloy (MA) the W-Cu composite elemental powders to reduce the W-W spacing and to super induce an interdiffusion layer on the elemental powders (Kecskes *et al.*, 2001 and Li *et al.*, 2006). So far all these techniques were not sufficient to attain fully dense, net shape compacts of these composite systems; furthermore, they bring along some negative impacts to at least one or two of the physical and mechanical properties of the sintered compacts such as conductivity, thermal expansion and strength. Another method and the most widely used one now is to infiltrate the sintered and porous W skeleton preforms by copper melt. The aim of all these processes is to achieve a homogeneous pore free MMC material with even distribution of the Cu phase in the W composite structure (Ho *et al.*, 2007).

## **1.2 Importance of Study**

So far, hundreds of researches and studies covered the sintering and densification of W-Cu composite materials; the majority of these researches were devoted to highlight some ambiguous sides which had been overshadowing the sintering of tungsten-copper composites for decades. However, despite all these tremendous efforts, some sintering features are still puzzling material community. Moreover, for sintering of tungsten-bronze composites, the research work are not well developed yet and there are very few publications available, most of the conducted works are limited to undisclosed patents and confidential researches (Kenneth, 2004).

### 1.3 Problem Statement

Alloying of W and bronze proves to be difficult to cast. The assessed equilibrium phase diagrams reveals that the two metals are almost completely immiscible in both solid and liquid phases ( $3 \times 10^{-5}$  wt.% at  $1300^\circ\text{C}$ ). This limitation excludes the use of conventional alloying techniques to develop fully-dense W-bronze alloys. Cu heat of mixing with W is positive i.e.  $35.5\text{kJ/mole}$  (Das *et al.*, 2008). Energy of formation of W-Sn solid solution is positive as well i.e.  $20\text{kJ/mole}$  (Xia *et al.*, 2006). The low solubility of W in bronze makes the contribution of solution reprecipitation is negligible, so densification can be attributed to either rearrangement or solid-state sintering. During LPS, bonding of W grains and the formation of W network skeleton slow densification and result in low sintered density for liquid phase contents as high as 35 vol. % or more (Johnson *et al.*, 2005a). High liquid phase volume fraction is necessary for better grain rearrangement and pore filling. However, the large density difference (over  $10\text{g/cm}^3$ ) between tungsten and liquid matrix enhances distortion and slumping by inducing severe solid settling and solid-liquid segregation (Wu *et al.*, 2003). Therefore, full densification and shape retention are two conflict matters. The difference between W and bronze melting temperatures (over  $2400^\circ$ ) add another complexity, sintering at relatively high temperature (above  $1300^\circ\text{C}$ ) leads to evaporation and weight loss of the matrix elements (Ozer *et al.*, 2007). Accordingly, attaining full densification or nearly full densification by conventional sintering of this system is a rather difficult task. So far, multiple approaches have been utilized to improve the sintered density of W-bronze systems. Recently new techniques have been adopted to enhance densification of this composite system such as enforced infiltration, coating of the W base particles by Ni element and to employ activation sintering by transition element

addition or by mechanical alloying. Still, additional new approaches need to be implemented to tackle W-bronze densification problem. This study is a contribution in this direction.

#### **1.4 Objective of Study**

The objectives of this work are:

1. To study the effects of the main sintering parameters namely sintering temperature, sintering time and sintering conditions (e.g. sintering atmosphere) on the densification of different W-pre-mix bronze and W-pre-alloy bronze compositions.
2. To study the effects of Fe and Co transition elements addition as sintering activators on the densification and microstructures of W-pre-mix bronze and W-pre-alloy bronze at different sintering temperatures and furnace atmospheres.
3. To investigate the effects of MA using different ball milling techniques, sintering activators and sintering conditions on the densification of W-bronze.
4. To explore and implement a new “full densification technique” based on the differential coefficients of thermal expansion ( $\Delta CTE$ ) between the W-base and the bronze component to induce compression stress helps in densification enhancement.
5. To conduct microstructural, physical and mechanical characterization of the W-bronze composite structures, yielded from various sintering techniques of this study.

## 1.5 Scope of the study

This study includes the application of five main sintering techniques. The main goal stands behind adopting these sintering techniques is to improve densification and to attain fully dense or near fully dense homogenous sintered structure of W-bronze composite. Implementation of new approaches and sintering concepts besides control and optimization of the sintering parameters lead to densification enhancement and eventually to porosity free fully dense structure. These five techniques include.

- § Liquid phase sintering at relatively high temperatures, above Cu melting temperature ( $1085T_m$ ).
- § Sintering at low temperatures i.e. between the solidus and liquidus temperatures of bronze (SLPS).
- § Activation sintering by transition metals addition, wherein small amounts of Fe and Co elements (1-5 wt %) is added to the W-bronze powder mix pre green compaction process.
- § Activation of the sintering process by mechanical alloying of the raw powder components and splitting of the ball milling process to two stages gives an advantage of manipulation the softness of Sn element to coat the hard W particles and to enhance the reaction affinity of W with the bronze matrix.
- § Implementation of new shell-on-core densification technique, wherein the differential coefficient of thermal expansion (CTE) between the hard W base and the bronze matrix is the driving force for densification process.

Other secondary goal is to characterize and assess the suitability of the outcome sintered compact materials for various industrial applications, the assessment includes; mechanical properties such as anti wear resistance and transfer rupture strength (TRS), physical properties such as the CTE and the resistivity values. The corrosion rate of the sintered compact was assessed by immersion corrosion test. Finally great attention has been paid to the sintering atmosphere due to its outstanding effect on the sintering products.

## **1.6 Structure of the Thesis**

In this thesis the back ground theory and the relevant literature survey are presented in the second chapter. This is followed in chapter three, by a description of all of the methods and techniques used in experiments, characterization and test procedure. Chapter four consists of the details of the results and discussions. Chapter five presents the conclusions of this thesis and the suggestions for future work.

## **CHAPTER 2**

### **LITERATURE REVIEW**

#### **2.1 Powder Metallurgy**

Powder metallurgy (PM) is a forming and fabrication technique consisting of three major processing stages. First, the primary material is physically powdered, divided into many small individual particles. Next, the powder is injected into a mold or passed through a die to produce a weakly cohesive structure via cold welding. Net-shape or near-net-shape fabrication is a key objective in many PM applications. Pressures of 1-8 tons per square cm are commonly used. Finally, the end part is formed by applying pressure, high temperature, long setting times (during which self-welding occurs), or any combination thereof. Two main techniques used to form and consolidate the powder, are sintering and metal injection molding. Many attributes contribute to the success of PM. Those include economical production of complex parts, fabrication below the melting temperature, eliminates segregation and other defects usually associated with casting process and the unique property or microstructures justification like porous metals, oxide dispersion strengthened alloys and combining non miscible metals. The inability to fabricate these unique microstructures by other techniques has contributed a lot to the growth of PM technology (Lee *et al.* 1998).

#### **2.2 Liquid-Phase Sintering (LPS)**

Sintering is the bonding together of particles at high temperatures. It can occur at temperatures below the melting point by solid-state atomic transport events.

In two phase systems involving mixed powders, it is possible to form a low melting phase. In such system, the liquid may provide rapid transport and therefore rapid sintering if certain criteria are met. Wetting is the first requirement, as the liquid must form a film around the solid phase.

Typically, LPS begins by mixing two or more small powders of different compositions. On heating, one powder melts or reacts to form a liquid between the particles that engulfs the more refractory phase. If the particle size is small, then capillary forces from the wetting liquid enhance densification (Hwang *et al.* 1987). The process consists of several overlapping steps involving solid state diffusion, particle rearrangement, solution-precipitation and solid skeleton densification (Johnson and German 1996). After sintering, the product is a composite of grains that were solid during sintering interlaced with a solidified liquid. An advantage from liquid phase comes when the particles are small and the liquid is wetting, in case of immiscibility between composite components as in W-bronze, the shrinkage is mainly confined to particle rearrangement (Liu and German, 2001).

Grain rearrangement upon liquid formation is the most important stage if rapid sintering densification is to be attained in practice. A liquid enhances sintering densification due to the inter-particle capillary force. Once a wetting liquid forms it penetrates existing solid-liquid boundaries and forms a pendulous bonds that provide a capillary force on the grain contacts. This capillary force results in sintering force that causes grain rearrangement, densification and contact flattening. The degree to which the liquid wets the solid grains determines the mode of liquid-phase sintering. If the quantity of the liquid is small or the solid grains are not wetted by the liquid, then bonding will be mainly by solid state diffusion i.e. conventional sintering. If the grains are spherical and completely wetted by liquid, the full densification is



theoretically possible by grain arrangement. Effort has been made to explain and quantify the process of grain rearrangement. On liquid formations, grain rearrangement, occurs due to the uneven capillary force exerted by the liquid on the solid grains. Accordingly, grain rearrangement is theoretically a function of multiple and random of capillary forces network (Liu and German, 2001).

Johnson and German, (1996) studied the solid-state and liquid-phase densification mechanisms of W-Cu sintered under different temperatures and sintering conditions, with and without Ni activator addition. Computer simulation was constructed to predict the densification behavior and concurrent microstructural development of liquid phase sintered composites for realistic heating cycles. The approach proposed the densification via grain shape accommodation to occur in three stages; initial, intermediate, and final, analogous to activated solid-state sintering.

### 2.2.1 Initial Stage.

Relying on Kingery (1959) assumption of concentration gradient at neck region being due to compressive stress in the liquid caused by capillary forces, Johnson and German (1996) proposed.

$$S^2 \frac{dS}{dT} = \frac{8\delta DC\gamma_{sl}\Omega}{kTG^4T'} \quad 2.1$$

where  $S$  is the linear shrinkage,  $dT$  is the temperature increment,  $G$  is the grain diameter,  $\delta$  is the width of the liquid interboundary layer,  $D$  is the diffusivity of the solid through the liquid layer,  $C$  is the atomic fraction of the solid in the liquid,  $\gamma_{sl}$  is the solid-liquid surface energy,  $\Omega$  is the vacancy volume,  $k$  is Boltzmann's constant,  $T'$  is the instantaneous heating rate. Solid-state sinter bonding occurs during

heating prior to liquid formation, but these bonds dissolve and reform contacts once the liquid becomes saturated with dissolved solid as shown in Figure. 2.1. Since curvature gradients are quickly dissipated via rapid mass transport through the liquid, equation 2.1 is overestimates the densification of high solubility systems during LPS.

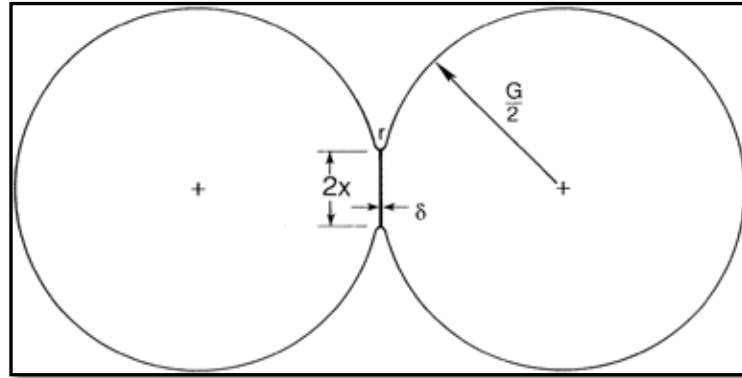


Figure 2.1: Two-particle geometry for predicting densification during the initial stage of liquid-phase sintering. The model considers mass transport through a liquid layer of thickness  $\delta$  with a grain size of  $G$ , a neck radius of  $x$ , and a curvature gradient at the neck of  $r$  (Johnson and German, 1996).

### 2.2.2 Intermediate stage

Dissipation of the curvature gradients of the neck region results in the formation of smooth interconnected pores at the grain boundaries. Densification is assumed to occur through a thin liquid layer at the grain boundaries. Schematics representation of the geometry is illustrated in Figure 2.2. The liquid tends to form rings around the interparticle necks. The pore curvature is the driving force for densification. Mass will be transported from the neck region so that the liquid can flow into the pore and the grain boundary. The governing differential equation for the intermediate stage can be obtained by combining Kingery's equation, heating rates and rate of change in porosity (equation 2.2).

$$(1 - \varepsilon - V_f) \frac{d\varepsilon}{dT} = \frac{-230\delta DC\gamma_{sl}\Omega}{kTG^4T} \quad 2.2$$

The densification resulting from both solid-state and liquid-phase sintering is based on the solid volume fraction, i.e., the fractional skeletal density. Only a small quantity of additive phase at the grain boundary is needed to enhance sintering. The rest of the additive phase fills a fraction of the pore space located between grains. The fractional skeletal density  $\rho_s$  and porosity are related by

$$\rho_s = 1 - \varepsilon - V_f \quad 2.3$$

Where  $\varepsilon$  is the rate of change of porosity and  $V_f$  is the volume fraction of the matrix.

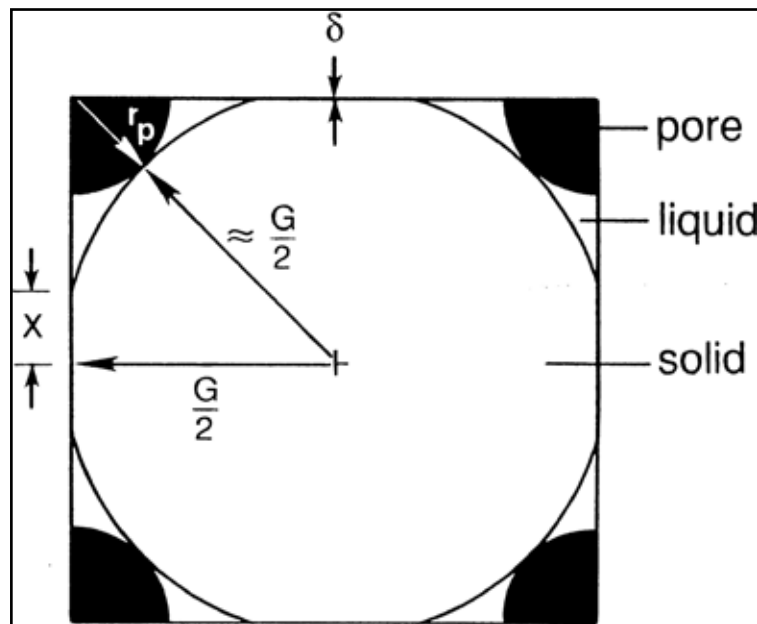


Figure 2.2: A cross-sectional view of the model microstructure for the intermediate stage of liquid-phase sintering (Johnson and German, 1996).

### 2.2.3 Final Stage

The pore closure begins early in the densification process, at densities as low as 50% of theoretical. Thus, the intermediate and final stage overlaps depending on the percentage of pores that are closed. These stages are considered simultaneously and are weighted according to the number of open pores versus closed pores. An expression relating the fraction of closed pores  $F_c$  to the fractional sintered skeletal density  $\rho_s$  was obtained by curve fitting of porosimetry data. The resulting empirical expression is

$$F_c = \exp \left( 9.242 - \frac{8.503}{\rho_s} \right) \quad 2.4$$

### 2.2.4 Grain Growth

Depending on the solubility of the solid in the liquid, Ostwald ripening results in significant grain coarsening during both the intermediate and final stages. The classic expression for grain growth via Ostwald ripening can be used under conditions of constant heating but is valid only for extremely dilute solid volume fractions. Modifications have been proposed by Johnson and German, (1996) to account for shorter diffusion distances and possible grain growth via coalescence associated with high solid volume fractions and overlapping diffusion fields. An earlier model (Glicksman and Vorhees, 1984) is used in conjunction with the empirical contiguity correction factor (Yang et al., 1990). The resulting expression is

$$\frac{dG}{dT} = \frac{648DC\gamma_{sl}V_s C \Omega}{27kTG^2T} \quad 2.5$$

Where  $V_s$  and  $C_v$  are the correction factors and the contiguity correction factor respectively.

### **2.3 Supersolidus Liquid-Phase Sintering (SLPS)**

A variant to traditional liquid-phase sintering is to use alloy powders, which are heated to a temperature between liquidus and solidus. During sintering process, the liquid forms inside the particles and spread to form pendular bonds at the particle contacts, resulting in capillary force acting on the semisolid particles. This process is termed SLPS (German, 1997). Densification is rapid once sufficient liquid forms to fragment the particles into individual grains. In this case, even large particles exhibit rapid densification. Observations on quenched particles show the liquid forms along grain boundaries, inside grains and at pendular bonds between particles. Liquid in the particles make the particles soft and easily deformed by grain sliding while liquid between particles generate a capillary force that induces densification. Liquid formation and densification events are related to the solid content and fractional coverage of grain boundary by liquid as summarized in Table 2.1. SLPS theory evolved from observations on particle fragmentation and microstructure evolution during densification. Viscous flow of the semisolid particles in response to capillary forces is the primary densification mechanism; the semisolid particles turn mushy and flow once liquid spreads along the grain boundaries. The viscosity decreases as the liquid volume fraction increases, so more liquid gives faster sintering. However, this lower viscosity leads to distortion. The fast transport rates in liquid also contribute to rapid grain growth. During isothermal sintering, the liquid spreads along grain boundaries, since less liquid is required to coat larger grains; thus, the semisolid system viscosity decreases due to grain growth coarsening.

Table 2.1: Liquid formation and densification events are related to the solid content and fractional coverage of grain boundary by the liquid (Lee, 1998).

Region	State	Approximate solid content	Typical fractional coverage	Behavior
I	Solid	1.00	0.00	Small densification, solid-state
II	Rigid	0.95 to 1.00	0.00 to 0.70	Slow, diffusional creep
III	Mushy	0.75 to 0.95	0.70 to 0.8	viscous flow, high viscosity
IV	Semisolid	0.60 to 0.90	0.8 to 0.90	rapid densification by viscous flow
V	Fluid-like	< 0.60	1.00	shape loss
VI	Liquid	0.00	-----	fluid

Temperature is the main controlling parameter; it controls the solid-liquid ratio, as illustrated in Figure 2.3, but not the microstructure softening. Densification depends on attaining a critical temperature (Tandon et al. (1995). Most SLPS

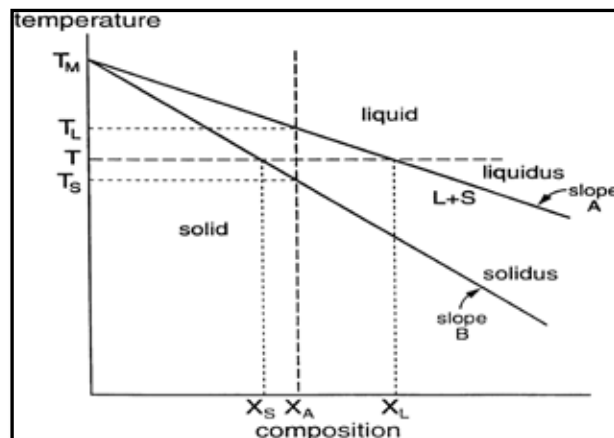


Figure 2.3: Schematic phase diagram showing the solidus and liquidus as straight lines, providing a simple means to estimate the effect of temperature on the liquid content and densification for an alloy of composition  $X_A$  in SLPS process (German, 1997).

Systems exhibit a step function when sintered density is plotted versus sintering temperature. Likewise, distortion follows closely behind densification, so often narrow sintering temperature ranges are required to obtain full density without distortion.

Most SLPS systems exhibit a step function between sintered density and sintered temperature. Consequently, distortion follows closely behind densification, so often narrow temperature ranges are available to obtain fully dense non distorted structure. The widespread implementation of powder atomization technologies capable of producing large quantities of alloy powders in the 20 to 250  $\mu\text{m}$  size range provides a new opportunity for SLPS. Normally, these powders are too coarse for use in traditional LPS, but they prove ideal for SLPS (German, 1997). Alloy powder particles formation during atomization technology is far from equilibrium solidification event, liquids might form at temperature 50°C lower than indicated by the phase diagram. For example atomized bronze powder (90Cu-10Sn) usually exhibits first liquid-phase sintering densification 25°C below the equilibrium temperature (German, 1997).

Assuming a linear relation between the liquidus and solidus temperatures and composition allows estimation of the solid volume fraction as a function of temperature. The solidus and liquidus temperatures ( $T_S$  and  $T_L$ ) change linearly with alloy composition  $X_A$  as follows.

$$T_L = T_M + AX_A \quad 2.6$$

$$T_S = T_M + BX_A \quad 2.7$$

Where  $T_M$  , is the baseline melting temperature as sketched in Figure 2.3;  $X_A$  is the alloying content on a weight basis,  $A$  and  $B$  are the slopes. With the assumed

linear relation, the compositions at the liquidus and solidus lines ( $X_L$  and  $X_S$  respectively) for any composition and temperature are given as.

$$X_L = \frac{T-T_M}{A} \quad 2.8$$

$$X_S = \frac{T-T_M}{B} \quad 2.9$$

The tie-line between these two compositions allows calculation of the solid mass fraction  $M_S$  for the particle at a given sintering temperature  $T$ .

$$M_S = \frac{X_L - X_A}{X_L - X_S} \quad 2.10$$

In turn, the volume fraction of solid  $\Phi$  depends on the solid mass fraction and the densities of the solid and liquid phases as follows.

$$\Phi = \frac{M_S/\rho_S}{M_S/\rho_S + (1-M_S)/\rho_L} \quad 2.11$$

Thus, for a given alloy composition and sintering temperature, the solid volume fraction inside the alloy particles can be calculated from the liquid and solid densities, if the solidus and liquidus temperature dependencies are known. However, for sintering of W-pre-alloy bronze, this explanation is relevant to the soft component i.e. the bronze matrix.

Liu *et al.*, (1995) studied the SLPS process and developed a two-particle model which takes into account an increasing liquid content with coalescence, particle shape changes and the variation in capillary force with processing parameters, such as temperature and liquid volume fraction. They introduces a numerical simulation of the capillary-force-induced particle coalescence showing the



geometric changes in the neck region and liquid phase profile as a function of relative shrinkage for large and small liquid volume.

## **2.4 Activated Sintering**

The manufacture of engineering metals and alloys in fabricated forms generally commences with the melting and casting of ingot material for subsequent shaping by mechanical techniques, such as forging, rolling and extrusion, although in many instances molten metal can be cast directly to a final shape. However, in the case of the refractory elements, such as tungsten and molybdenum, their very high melting points (in excess of 2000°C), as well as their resistance to deformation, generally precludes the melting approach as a practical route to material and component manufacture. This has led to the development of processes in which consolidation of powder materials is achieved by sintering at temperatures below their melting points. To promote and assist the sintering process, two techniques have been developed which involve the use of metallic sintering additives. These are known as Liquid Phase Sintering and Activated Sintering.

In Liquid Phase Sintering, the refractory metal powders are sintered in the presence of one or more metals, generally transition metals such as copper or iron at temperatures above the melting point of the additive, so that sintering occurs in a molten binder phase which may be present in substantial amounts, for example up to 40 per cent by weight. In contrast, activated sintering is performed in the presence of small amounts of metal additives, again often transition metals, but in the solid state at temperatures below the melting point of the additive. Activated sintering can be accomplished at lower temperatures than liquid phase sintering, although not necessarily so, depending on the particular metal additive used. In both cases,

however, the temperatures employed are substantially lower than would otherwise be required if the refractory powders were sintered without additives. For example (Kurtz, 1949) showed that 99% dense tungsten parts could be achieved by sintering below 1400°C with less than 1 wt.% addition of nickel, whereas temperatures above 2800°C are required to achieve a comparable density in untreated tungsten powder. Generally, activated sintering refers to several techniques which lower the activation energy, allowing for a lower sintering temperature, shorter sintering time, or better properties. Several techniques, ranging from metallic additions to the application of external electrical fields, meet the goal. Mixed phase sintering treatments can also be categorized as activated sintering.

#### **2.4.1 Activated Sintering by Transition Metals Addition**

Since Vacek, (1959) reported the enhancement of sintering by additions of small quantities of transition metals to tungsten in making it possible to lower the sintering temperature substantially, a great deal of work has been carried out into the activated sintering of W and other refractory metals. Early work on the activated solid-state sintering (SSS) of tungsten was carried out by Brophy et al., (1961) and Hayden, (1960). Their initial work focused on the sintering of tungsten powder coated with nickel. They found that, on sintering at 1100°C, the tungsten underwent rapid densification to more than 90% theoretical density (TD). Moreover they found that the amount of nickel required to promote this accelerated sintering was roughly equivalent to a nickel coating thickness of about one atomic monolayer. They attributed enhanced sintering to the formation of liquid by Ni. Early researches by Panichkina, (1966) and later ones by Li and German, (1983), Johnson and German, (1996), and Boonyongmaneerat, (2008) have demonstrated that addition of group

VIII transition metals including Ni, Co, Fe and Pd can beneficially enhance the sintering kinetics of W powder and thus reduce its sintering temperature. It was found that sintering additives which are insoluble in W can segregate to the W interparticle zone, provide a high diffusivity transport path for W atoms and consequently lower the activation energy for bulk transport of W (German and Munir, 1976). However, the majority of researches conducted so far on activated sintering of tungsten were on solid-state sintering of this element alone. Accordingly, relatively high sintering temperatures have been utilized (1100-2000°C). Even for those researches on activated LPS of W-Cu material, the sintering temperatures were at least above 1084°C which is the melting temperature of copper.

Panichkina, (1966) has studied the effect of introducing 0.5 wt. % nickel into tungsten. The coated tungsten was sintered at 1200°C, only few specimens were sintered at 1100°C. Shrinkage of specimens was observed at temperatures as low as 1100°C. The sintering process is not affected by the method of introduction of nickel. A W-Ni solid solution appeared during sintering along the grain boundaries. The results obtained in this study confirmed the results obtained earlier by Vacek (1959).

Toth and Lockington, (1967) carried out further work on activated sintering of tungsten by palladium and nickel; they found that there were optimum concentrations of both palladium and nickel for maximum densification during sintering at 1000°C. Palladium was found to be more effective than nickel especially at and below temperature of 950°C. Microprobe analysis of the fracture surfaces of sintered specimens showed segregation of the activating elements on grain boundaries. The authors concluded that Brophy's model (Brophy *et al.*, 1961) for activated sintering was not applicable; rather, they favored a mechanism in which the

surface diffusion of tungsten on the activator surface is the controlling step; both models are shown schematically in Figure 2. 4.

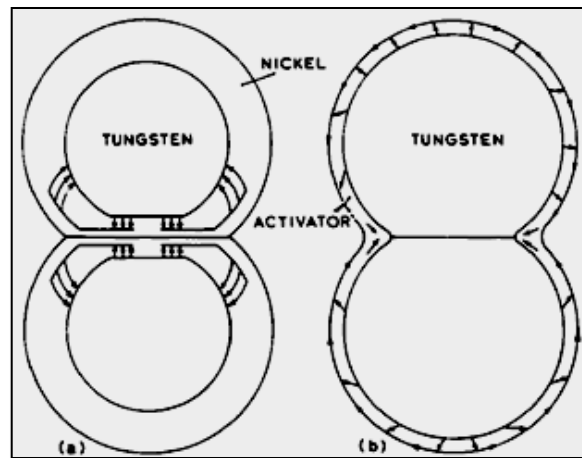


Figure 2.4: Two models of tungsten particles which have been coated with metallic activator, show different representations of the sintering process (a) Brophy, Hayden and Wulff model (b) Toth and Lockington model (Corti, 1986).

The model of Brophy *et al.*, (1961) has tungsten diffusing through the carrier (activator) phase, away from the line joining the centers of adjacent particles, to be re-deposited elsewhere on the particles as indicated by the arrows in Figure 2.4. (a). The model of Toth and Lockington, (1967), where dissolution of tungsten at the activator-tungsten interface is followed by volume diffusion outwards through the activator layer and subsequent surface diffusion, this being the rate controlling step. Diffusion through the activator layer to the contact point between adjacent particles results in the formation of sintering necks.

Samsonov and Yakovlev, (1966) explained the enhanced densification of tungsten by Ni addition by the filling of electrons in the d-orbital. The tungsten atoms acts as electron acceptors and the nickel atoms as electron donors; transfer of unlocalized electrons from nickel to tungsten results in an increase in the statistical weight of tungsten atoms having the energetically stable  $d^5$ -configurations and of

nickel atoms with stable  $d^{10}$ -configuration and in a decrease in the concentration of unlocalized electrons, i.e., in an energetic stabilization of the whole system. The resulting reduction in the total energy reserve of the system provides a moving force for the sintering. Samsonov and Yakovlev, (1968) in another study on the influence of iron-group metal additions on the sinterability of tungsten powder at temperatures of 1000-2000°C showed that the activating effect of these additions increases in the sequence  $Fe \rightarrow Co \rightarrow Ni$ .

German and Munir, (1976) extended this work to other Group VIII elements including platinum, and confirmed that enhanced sintering commenced at about 1 monolayer thickness and peaked at 4 monolayers. They found the effectiveness of the activator to be in the order  $Pd > Ni > Pt = Co > Fe > Cu$ , below 1300°C, iron was more effective than platinum and cobalt. Kaysser *et al.*, (1982) suggested the mechanism of plastic deformation. In other investigation Kaysser *et al.*, (1987), they reported that the grain boundary diffusion of W in Ni-doped W was increased 500 to 5000 times as opposed to that of undoped W.

Li and German, (1983) investigated the effects of powder characteristics, activators and processing variables on the shrinkage, and mechanical properties of tungsten compacts processed by activated sintering in the range 1200 to 1600°C. Soluble nitrates salts of Pd, Ni, Co and Fe were mixed with W powder in water, subsequently the water was evaporated and coating of four monolayer were deposited on powder particles, hardness level were in the order  $Pd > Ni > Co > Fe$  at lower temperatures, but were closer together at higher temperatures. In case of transverse rupture strength, nickel-activated tungsten was stronger than palladium-activated tungsten, the strength decreasing with increasing sintering temperature above 1400°C, was due to rapid grain coarsening.

Favorable systems for activated solid-state sintering of W can be identified through phase diagram characteristics including solubilities, melting temperatures, and intermediate phase relationships. The solubility of W in the additive should be much higher than the solubility of additive in W. This is necessary for both the solubility and segregation requirement as illustrated in Figure 2.5 and in Table 2.2. To ensure segregation, the liquidus and solidus should decrease with increasing additive concentration (German, 1992 and Johnson and German, 1993).

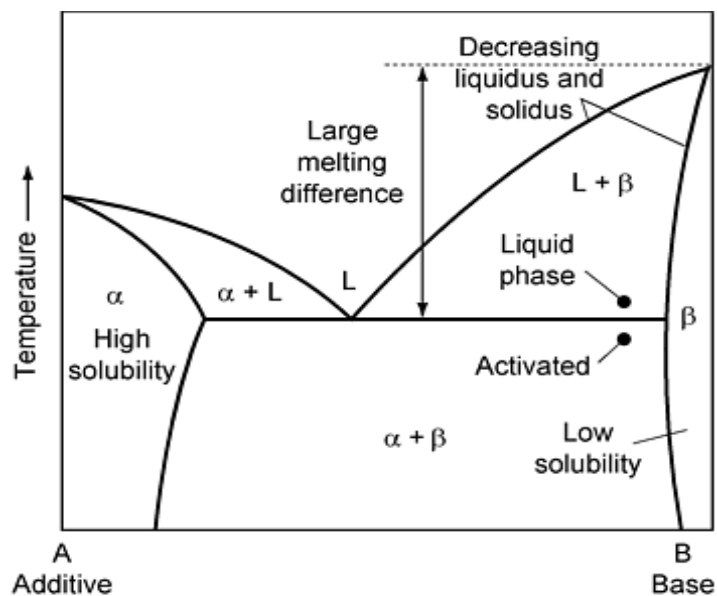


Figure 2.5: Phase diagram of an ideal system for liquid-phase sintering and metal activated sintering (German, 1992).